THE JOURNAL OF PHYSICAL CHEMISTRY C

Subscriber access provided by UNIV OF WISCONSIN - MADISON

C: Physical Processes in Nanomaterials and Nanostructures

Defects in Self-Assembled Monolayers on Nanoparticles Prompt Phospholipid Extraction and Bilayer Curvature-Dependent Deformations

Gene Chong, Isabel U. Foreman-Ortiz, Meng Wu, Anthony Bautista, Catherine J. Murphy, Joel A. Pedersen, and Rigoberto Hernandez

J. Phys. Chem. C, **Just Accepted Manuscript** • DOI: 10.1021/acs.jpcc.9b08583 • Publication Date (Web): 23 Oct 2019

Defects in Self-Assembled Monolayers on Nanoparticles Prompt Phospholipid Extraction and Bilayer Curvature-Dependent Deformations

Gene Chong[†], *Isabel U. Foreman-Ortiz*[‡], *Meng Wu*[§], *Anthony Bautista*[†], *Catherine J. Murphy*[§], *Joel A. Pedersen*[‡,∥], *and Rigoberto Hernandez**[†]

[†] Department of Chemistry, Johns Hopkins University, Baltimore, Maryland 21218, United States

[‡] Department of Chemistry, University of Wisconsin—Madison, Madison, Wisconsin 53706, United States

[§] Department of Chemistry, University of Illinois at Urbana—Champaign, Urbana, Illinois 61801, United States

[∥] Departments of Soil Science and Civil & Environmental Engineering, University of Wisconsin—Madison, Madison, Wisconsin 53706, United States

Abstract

Metal nanoparticles (NPs) functionalized with self-assembled monolayers (SAMs) of long alkanethiol ligands are subject to defects in the SAM structure due to the interplay between alkyl chain packing and free volume available in space per ligand. We find *via* dissipative particle dynamics (DPD) simulations that hydrophobic contact between protruding acyl chains of phospholipids from lipid vesicles and exposed alkyl chains in SAM defects prompts NP insertion and that defects become sites for phospholipid extraction. Experiments show that cationic (11-mercaptoundecyl)trimethylammonium bromide (MUTAB)-coated AuNPs, analogous to the models used for the simulations, attach to and acquire lipids from planar supported lipid bilayers, while anionic 11-mercaptoundecanoic acid (MUA)-coated AuNPs do not. Phospholipid extraction and the structure of the ligands inserted in bilayers collectively contribute to bilayer thinning at the site of NP insertion and bilayer-curvature dependent deformability, revealing how these typical engineered SAM-coated NPs interface with lipid-bilayer systems with potential biological consequences.

1. Introduction

Metal nanoparticles (NPs) have shape- and size-dependent optical and electrical properties for applications in energy storage,[1] imaging,[1-2] molecular sensing,[3-4] and photothermal therapy.[5-6] Once synthesized, NPs are typically functionalized with ligands to protect the inorganic core and achieve colloidal stability and uniform dispersion in aqueous suspensions or thin films.[7] Self-assembly of alkanethiol monolayers on NP surfaces is a common means of functionalization.[8] Gold nanoparticles (AuNPs) in particular are biologically inert; their biocompatibility coupled with the their plasmonic properties makes AuNPs an ideal choice for biomedical applications such

as sensing[3-4] and targeted therapeutic[5,9] agents. The synthetic control over AuNP shape, size, and surface ligand chemistry also enables the use of AuNPs as models to probe how the resulting self-assembled monolayer (SAM) of ligands on NPs—whether functionalized for biological applications, or other technological devices that might be discarded into the environment at end of life—interfaces with biological systems.[10]

Simulation and experiment in tandem have helped identify specific ligand structures and properties that trigger events initiated at the interface between AuNPs and lipid bilayers such as NP binding, NP translocation, and cell lysis. All-atom molecular dynamics (MD) simulations[11-12] have shown that cationic alkanethiol-coated AuNPs interact more strongly with planar membranes than anionic alkanethiol-coated AuNPs because the cationic ligands can penetrate more deeply into the membrane and access the anionic phosphates in the lipid head groups. At larger biologically relevant scales, experiments observing reduced bacterial colony count and cell lysis have demonstrated[13-14] that cationic AuNPs are generally more toxic, potentially due to stronger association of cationic AuNPs with the cell envelope, albeit in a varied set of membranes that do not all consist exclusively of lipids. Interestingly, MD simulations of lipid bicelles[15] and MARTINI coarse-grained simulations of membranes[16] with 2 nm diameter AuNPs protected by mixed ligand layers of anionic alkanethiols and uncharged methyl-terminated alkanethiols have shown that anionic AuNPs can also insert into these zwitterionic lipid-bilayer systems. These results suggest that association of NP ligands with lipid bilayers is independent of the ligand charge provided that parts of the hydrophobic alkyl chains in both the ligands and the lipids are solvent-exposed and in sufficient proximity to interact.

In essence, the morphology of the self-assembled monolayer (SAM) of ligands on NPs drives the interaction of NPs with amphiphilic biomolecules. Simulations of the nano-bio interface

have largely focused on defect-free SAMs on NPs for functionalized NP models. That is, the force-field parameters for NP ligands have been tuned,[17-18] or mixtures of charged and uncharged ligands, each with different lengths, have been used[15-16,19-20] to generate SAMs with uniform spatial distribution of ligands on NPs. The even distribution of hydrophilic and hydrophobic coarse-grained beads on a spherical NP surface also represents defect-free SAMs on NPs.[21-23] In recent work, a combination of solution ^{1}H-nuclear magnetic resonance (NMR) spectroscopy and MD simulations was used to determine the SAM structure of the alkanethiol (11-mercaptoundecyl)trimethylammonium bromide (MUTAB) (Fig. S1 in SI) and of the 16-carbon variant (MTAB) and the nature of defects in SAMs. Ligand density and AuNP size were varied and correlated with changes in NMR chemical shifts of the terminal quaternary ammonium headgroup protons.[24] Long-chain alkanethiols assemble into loosely ordered ligand islands particularly on AuNPs with core sizes < 8 nm due to the high NP surface curvature and competition between hydrophobic ligand chain packing and free volume available in space per ligand. This leaves defects in the SAM, or voids in space where the charged ligand headgroups would reside if they were uniformly distributed within the same spherical shell, and exposes the hydrophobic chains between ligand islands (Fig. 1A). This ligand-island morphology on AuNPs has previously been revealed *via* MD simulations by other groups[25-28] and is predicted to form among ligands with alkyl chain lengths exceeding four –CH_2 groups.[26] Such ligand-island morphology has also been observed both experimentally and computationally in NPs of other metal chalcogenide and noble metal cores: CdSe,[29] PbS,[30] and silver.[31]

Here, we probed the association of AuNPs functionalized with either cationic MUTAB or anionic 11-mercaptoundecanoic acid (MUA) ligands (Fig. S1 in the SI) with zwitterionic phospholipid bilayers computationally by dissipative particle dynamics (DPD) simulations using

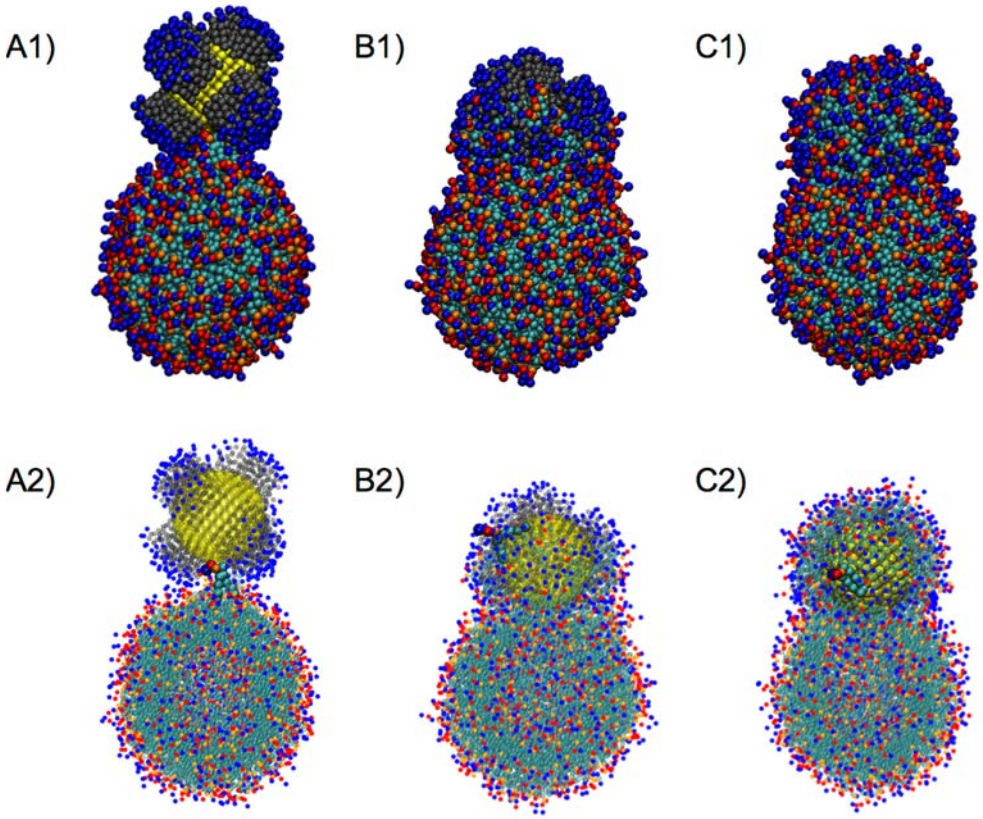

Figure 1. Mechanism for nanoparticle (NP) membrane insertion and the onset of phospholipid extraction by a protruding phospholipid acyl chain (shown in solid beads in row 2): A) NP insertion starts upon a spontaneous lipid-tail protrusion event at which point we reset the timer to t=0. Lipid-tail protrusion enables interaction with exposed hydrophobic chains on the edges of ligand islands; B) A ligand island inserts into the vesicle, and lipids shuttle up the NP along defects between ligand islands, shown 20,000 timesteps or ~2 μs after the lipid-tail protrusion event; C) The nanoparticle has inserted, and the ligand layer is saturated and mixed with lipids, shown 200,000 timesteps or ~20 μs after the lipid-tail protrusion event. In row 1, all coarse-grained beads are shown to scale with gold beads in yellow, hydrophobic beads of the NP ligands in gray, hydrophobic beads of the lipids in cyan, lipid glycerol groups in orange, lipid phosphate groups in red, and quaternary ammonium groups of both the lipids and NP ligands in blue. In row 2, all beads, except for the initial protruding lipid, are made transparent with smaller bead size. Water beads are removed for clarity in both rows.

bottom-up coarse-grained NP models and experimentally by quartz crystal microbalance with dissipation monitoring (QCM-D). We modeled 4 nm MUA- and MUTAB-AuNPs in the simulations. The QCM-D experiments were performed on 4 nm MUA-AuNPs and 8 nm MUTAB-

AuNPs. We used 8 nm MUTAB-AuNPs in experiments because we found 4 nm MUTAB-AuNPs to not be consistently colloidally stable by comparison. We confirm the hypothesis that NPs with SAM defects —that result from the formation of ligand islands on 4-8 nm AuNPs[24]—interact favorably with phospholipid bilayers through a mechanism of phospholipid extraction. The nature and size of the ligand islands (*e.g.* number of ligands per island, number of islands, ordered packing of ligands within islands) and surrounding defects in the SAM are highly dependent on AuNP size, ligand length, and ligand headgroup chemistry.[24,26-28] Further, this work reveals a mechanism for NP insertion, lipid extraction, and bilayer thinning driven by defects in SAMs on smaller NPs (Fig. 1).

2. Materials and Methods

2.1. Dissipative Particle Dynamics (DPD) Simulations.

Three heavy atoms were mapped to one coarse-grained bead with a bead volume of 90 Å^3. Ligands were grafted on a spherical NP shell (Fig. S1 in the SI), and 1,2-dimyristoyl-*sn*-glycero-3-phosphocholine (DMPC) lipids were modeled using force-field parameters modified from those developed by Smit and co-workers,[32] which were previously benchmarked using all-atom simulations of DMPC-lipid bilayers. We also incorporated electrostatic interactions[33] into the DPD simulations. The mapping scheme and bead volume resulted in a ligand density of 4.8 molecules/nm^2 in agreement with NMR experiments.[24] Specifically, 242 ligands were grafted uniformly to cover a 4 nm spherical surface with grafting points fixed as a rigid body and the rest of the ligands able to move freely to represent the ligand-coated 4 nm NPs with 2123 Au atoms used in our previous all-atom simulations.[24] 1,2-dioleoyl-*sn*-glycero-3-phosphocholine (DOPC) lipids were used for QCM-D experiments, as reported below. DOPC and DMPC lipids possess the

same phosphatidylcholine headgroups and differ in acyl chain length (18 carbons for DOPC, 14 carbons for DMPC) and degree of saturation (the acyl chains in DOPC each contain a single unsaturated bond; the acyl chains in DMPC are saturated). At the coarse-grained scale, the differences between the phospholipids are minimal. Bilayers composed of each phospholipid have similar thickness, density profiles of lipid functional groups across bilayers, and elastic properties.[34-35] We constructed a 12 nm, 576-DMPC lipid vesicle and a 25 nm, 4000-DMPC lipid vesicle model *via* self-assembly simulations[35] to simulate with 4 nm MUTAB- and MUA-NPs. Force-field parameters and system-size information are provided in Tables S1-3.

For each simulation, the gold core of the NP moved as a rigid body with its center of mass initially attached to a spring at the center of the simulation box, allowing it to move up to 2 nm (the NP radius) from this position. The vesicle was free to move in the simulation box. Box sizes were chosen such that half of a box length was the sum of the radius of the NP, the diameter of the vesicle, and a 13 Å water cushion. Thereby, the NP did not interact with the periodic image of the vesicle. Counterions were included so that the salt concentration of the box was 0.1 M. We observed that lipid-tail protrusion is the first step in the insertion of NPs into bilayers (Fig. 1A), as previously identified with 2 nm AuNPs on curved edges of bicelles[15] and on planar membranes.[16] At the first onset of lipid-tail protrusion in which the lipid tail moves out of the plane normal to the bilayer and into solvent, simulations were restarted with constraints on the NP removed. The small vesicle models used in our simulations allowed us to understand the influence of vesicle size effects on their structural transformations upon NP insertion and accelerate the lipid-tail protrusion event which still did not occur consistently in these conditions and otherwise would occur at timescales difficult to access computationally on planar membranes.[15-16,19] The behavior on a planar surface would be the subject of a different investigation because it would require different

techniques to address the differences in its macroscopic topology. We ran a series of simulations of up to 10,000,000 timesteps or ~10 μs and obtained five trajectories each of MUTAB- and MUA-NPs with a 12 nm vesicle and three trajectories of MUTAB-NP with a 25 nm vesicle, in which a protruding phospholipid tail comes in contact with a NP ligand chain.

Packmol[36] was used to generate the initial configurations for each simulation. All simulations were run using LAMMPS[37] at a timestep of 0.02τ with the reduced time unit τ and at constant NVE. A timestep is on the order of 100 ps.[22,38-39] The DPD thermostat was set to the reduced temperature $T^* = 1$. Short- and long-ranged electrostatic interactions were calculated through the particle-particle particle-mesh (PPPM) method.

2.2. Quartz Crystal Microbalance with Dissipation Monitoring (QCM-D) Experiments.

We used a QSense E4 QCM-D module (Biolin Scientific) with SiO_2-coated QCM-D crystals (QSX303) to monitor the formation of phospholipid bilayers and subsequent interaction with MUA- and MUTAB-AuNPs. The synthesis and characterization of MUA- and MUTAB-AuNPs are described in the Supporting Information. Supported 1,2-dioleoyl-*sn*-glycero-3-phosphocholine (DOPC) bilayers were formed by the vesicle fusion method.[40] Briefly, small unilamellar vesicles formed in 0.001 M NaCl were diluted to 0.125 $mg \cdot mL^{-1}$ in 0.1 M NaCl. This diluted vesicle mixture was first flowed over bare SiO_2-coated sensors until rupture and fusion, followed by subsequent rinsing with buffers of lower ionic strength (0.01 M NaCl, then 0.001 mM NaCl), all at 100 $\mu L \cdot min^{-1}$. In the case of MUTAB-AuNPs, a 0.25 M NaCl solution was used to further encourage vesicle rupture, and was applied after 0.10 M NaCl subsequent to vesicle rupture. Ionic strength was then lowered sequentially as before. AuNPs were diluted in 0.001 M NaCl to a number concentration of 10 nM and subsequently flowed over the bilayer for 30 min at 50 $\mu L \cdot min^{-1}$. This was followed by a 30 min rinse with 0.001 M NaCl at 50 $\mu L \cdot min^{-1}$ for 30 min.

Resultant QCM-D graphs for MUA- and MUTAB-AuNPs are reported in Fig. S4 in the SI, where vesicle and buffer rinse steps are labeled.

We examined the hydrodynamic and electrokinetic properties of AuNPs after they had passed through the QCM-D flow cell. Effluent from the QCM-D flow cell was collected that corresponded to the first 15 min of the rinse phase after nanoparticle attachment. AuNPs were collected at an identical timepoint (during subsequent buffer rinse) when flowed over bare SiO_2-coated sensors. These fractions were characterized by DLS and laser Doppler microelectrophoresis to assess possible changes in hydrodynamic size or apparent ζ that might reflect extraction of DOPC from the bilayers.

3. Results and Discussion

3.1 DPD Simulations and Discovery. We find that SAM defects on NPs not only prompt NP insertion into bilayers, but also become sites for phospholipid extraction from bilayers (Figs. 1B, and S8-10 in the SI). Due to the degree of curvature in the modeled vesicles or the presence of an underlying solid support in QCM-D experiments, reported below, we observed the attachment of the anionic MUA-AuNPs to vesicles, which was not observed in the experiments on planar bilayers. In the latter case, defective, budding, or curved regions in the bilayer are required to expose lipid tails for anionic AuNP insertion, as shown in previous experiments.[13,15] Nevertheless, simulations with MUA-AuNPs can be used to analyze the transformations driven by hydrophobic interactions between exposed ligand chains and lipid tails at the NP-bilayer interface. At the end of each trajectory, we identified a ligand that had inserted into the vesicle and tracked its distance from the center of mass (COM) of the vesicle (vesicle COM) over time, starting from the initial phospholipid acyl chain protrusion event set as $t = 0$ (Fig. 2A). The ligand was initially oriented ~63-84 Å away from the vesicle COM, or ~3 to 24 Å from the 12 nm vesicle surface,

exposing the hydrophobic chains on the edges of its associated ligand island toward the vesicle. The converged distance between the tagged ligand and vesicle COM fluctuated around an average of 24.9 Å. The NP appeared to remain inserted and extracted phospholipids *via* the shuttling of phospholipids near the site of ligand-island insertion to surrounding regions in the SAM with exposed hydrophobic ligand chains. A similar phenomenon has been observed in all-atom MD simulations in which phospholipids shuttled along carbon nanotubes inserted into bilayers, and facilitated cellular uptake as imaged through transmission electron microscopy.[41]

At the coarse-grained level of these simulations, a timestep cannot be rigorously mapped to real time units.[42] An effective coarse-grained time can be obtained by matching the lateral

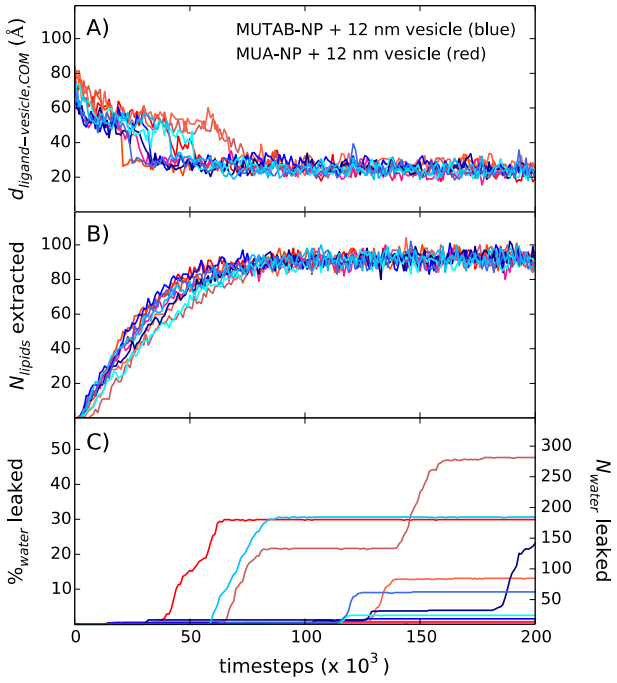

Figure 2. A) Distance between NP ligand and vesicle COM, $d_{\text{ligand-vesicle,COM}}$ *vs.* time; B) Number of lipids, N_{lipids}, extracted *vs.* time; and C) Percent of water beads, $\%_{water}$, and number of water beads, N_{water}, leaked from vesicles *vs.* time. Note that each trajectory started with 585 water beads inside the vesicle core. In each panel, the results from five trajectories with cationic MUTAB-NPs and 12 nm vesicles are shown in blue and from five trajectories with anionic MUA-NPs and 12 nm vesicles in red. The phospholipid-tail protrusion event is set as 0 timesteps.

diffusion coefficient of lipids in DPD simulations with experimental values. Through the correspondence to the lateral diffusion coefficient (5 $\mu m^2/s$) for lipids with similar structure to DMPC, the resulting estimate of the DPD timestep is on the order of 100 ps.[22,38-39] The time to NP insertion is 25,000-75,000 timesteps, or on the order of 2.5-7.5 μs after the spontaneous phospholipid-tail protrusion event (Fig. 2A), and the time to saturation of SAM defects with ~92 phospholipids extracted from the 12 nm vesicles is 100,000 timesteps, or on the order of 10 μs (Fig. 2B). The fluctuations around the average number of lipids extracted suggest that lipids can still move between the membrane and the SAM, once the NP has inserted. The corresponding results with the 25 nm vesicle are provided in the Supporting Information. The NP insertion time into 25 nm vesicles varies greatly from 25,000-175,000 timesteps across the trajectories for the 25 nm vesicle, or on the order of 2.5-17.5 μs after the phospholipid-tail protrusion event (Fig. S7). As such, the lower-curvature and larger 25 nm vesicles resemble nearly planar membranes with respect to the barriers to penetration that they present to particles less than 10 nm in diameter. Approximately 93 lipids are extracted from the 25 nm vesicle, similar to 12 nm vesicles, due to the fixed ligand density on the NPs.

The number of phospholipids extracted and the percent of water beads leaked from vesicles were determined by first computing the radial distribution functions, $g(r)$, between the NP COM and lipid glycerol beads and between the vesicle COM and glycerol beads, respectively (Figs. S5-6 in the SI). We used the distance at the half-maximum after the respective peak in the $g(r)$ as cutoffs to count the gain in lipids within the cutoff around the NP COM, excluding the portion of the NP inserted in the vesicle, and loss of water within the cutoff around the vesicle COM. We observe no consistency in the amount of water leaked from vesicles upon NP insertion across the trajectories and attribute high leakage (> 10%) to deformations in 12 nm vesicles due to the high

bending moduli of smaller vesicles with higher curvature.[43-46] Leakage of 0-60 water beads is more consistent with results from simulations using the larger 25 nm vesicles (Figs. 2C, and S7 in the SI). Even in the dilute limit of a single NP and vesicle, we found that NP association can lead to water leakage as has been observed in experiments involving fluorophore release from vesicles.[13,47]

We also find that ligand-island insertion, phospholipid extraction, and ligand length collectively cause bilayer curvature-dependent transformations. We calculated the absolute value of the difference in the radial coordinates relative to the vesicle COM of the glycerol bead and final acyl chain bead, and took the average value between the two acyl chains per lipid to determine the lipid acyl chain end-to-end distance, r_{ee}, for each lipid in the vesicle. The distribution of r_{ee}, in essence, captures the local packing and tilting of lipids throughout the vesicle in response to NP exposure (Figs. 3, and S11-13 in the SI). Vesicles in the size range of ~10 nm are generally metastable and readily fuse with other vesicles to make larger ones.[43-44] Moreover due to the high bending resistance of highly curved vesicles,[45-46] we find that the 12 nm vesicle buckles and the bilayer becomes less locally curved, as shown in Figs. 3A, 3B, and S11-12 in the SI. Figs. 3C and 3F illustrate the reconfiguration of the lipid bilayer around the inserted ligand island and surrounding defects. The bilayer becomes thinner, *i.e.* decreases in thickness, as lipids tails splay near the NP insertion site. This is quantified by an increase in blue markers signifying smaller r_{ee} and a shift in the distribution of lipids in the inner layer from 3 to 4 nm away from the 12 nm vesicle COM and from 9 to 11 nm away from the 25 nm vesicle COM (Figs. 3, and S11-13 in the SI). This decrease in bilayer thickness is common to both the 12 nm and the larger 25 nm vesicle though the latter is subject to less deformation due to the fact that it is necessarily less curved *a priori*. In both cases, the bilayer decreases in thickness such that hydrophobic contact between the

lipid bilayer (10 hydrophobic beads across) and ligand chains (four hydrophobic beads) are maximized and that the hydrophilic terminal groups of the ligands penetrate to the water inside the vesicle. The global thinning in the spatial distribution of lipids in the outer layer of the 12 nm and 25 nm vesicles, as lipids in the outer layer become more ordered upon NP insertion was also seen in plots of the lipid distribution when normalized by the annular areas as can be seen in Fig. S14 of the SI. Longer time-scale results beyond 1,000,000 timesteps are also presented in the SI, and provide confirmation that these are converged structural transformations.

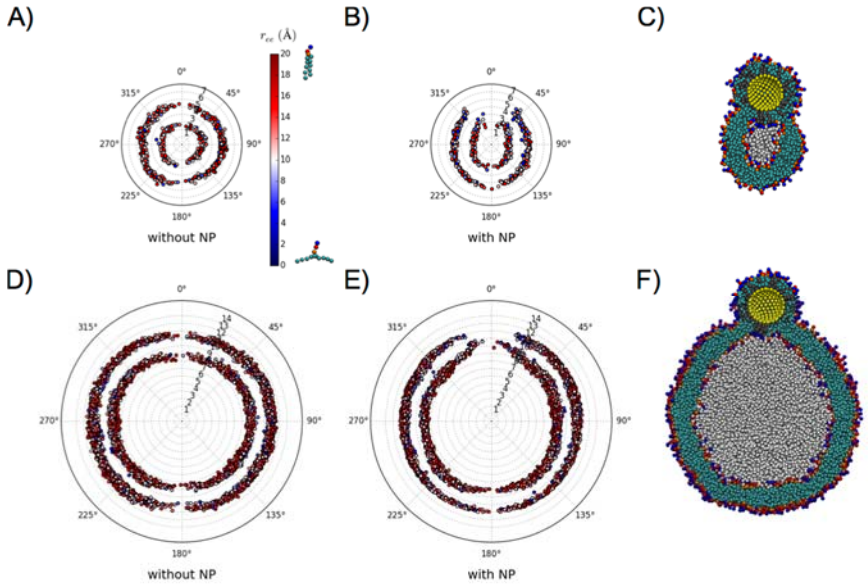

Figure 3. Distribution of lipid glycerol groups and the average lipid acyl chain end-to-end distance, r_{ee}, for each lipid for 12 nm (in panels A and B) and 25 nm (in panels D and E) vesicles without the presence of a NP and in the presence of the NP 200,000 timesteps after the lipid-acyl chain protrusion event upon NP exposure. The trajectory snapshots in panels C and F show the corresponding cross sections of the NP inserted in the vesicles. The color of a given point in panels A-B and D-E indicates the r_{ee} as per the color bar shown next to panel A. A high r_{ee} is indicative of lipid tails oriented perpendicular to the plane of a bilayer, and a small r_{ee} is indicative of lipid tails either splayed or with greater tilt within the bilayer. Vesicles are oriented with the COM at 0 nm and the NP insertion site at the 0° pole. Lipid distribution is plotted in 1 nm radial ticks relative to the vesicle COM invariant of the equatorial angle, and therefore, fewer points are sampled at the poles compared to the equator. Please refer to Fig. S14 to the polar invariant plots corresponding to panels A, B, D and E.

3.2 QCM-D Experiments & Validation. AuNPs were flowed over supported lipid bilayers made up of DOPC lipids in QCM-D experiments. MUA-AuNPs were not observed to attach to or extract lipids from bilayers (Figs. 4A, 4B, and S15A in the SI). MUTAB-AUNPs appeared to extract lipids from the bilayer as evidenced by the change in the hydrodynamic properties of the nanoparticles exiting the QCM-D flow cell during rinsing relative to those exiting flow cells housing bare SiO_2-coated sensors (Fig. 4C). The MUTAB-AuNPs interacted strongly

with both the DOPC bilayer and the SiO_2-coated sensor, but only in the case of the bilayer is a decrease in acoustic mass evidenced (reflected as an increase in frequency in Fig. S15B in the SI). The loss of mass corresponds to release of nanoparticles and associated lipids from the surface of the bilayer-coated sensor. The pronounced aggregation of the MUTAB-AuNPs released from the bilayer-containing flow cells relative to those flowing through flow cells housing bare SiO_2-coated sensors indicates a change in surface properties induced by interaction with bilayer and may reflect extraction of lipids from the bilayer. In addition to the extraction of these phospholipids, other interactions between MUTAB-AuNPs and the bilayer could include the removal of MUTAB ligands by the bilayer and ligand-lipid exchange.[48] These latter two cases would lead to a cumulative loss of cationic MUTAB ligands and gain of anionic lipid phosphate groups, respectively, both significantly lowering the apparent zeta potential (ζ-potential). The ζ-potential did not differ between particles that were released from bilayers and those that transited flow cells containing bare SiO_2-coated sensors, suggesting that the major interaction is lipid extraction by MUTAB-AuNPs (Fig. 4D).

While the QCM-D experiments reveal NP attachment to and transformation on lipid bilayers—useful in general, and for benchmarking our simulations, in particular—they cannot provide the detailed structure and dynamics available from all-atom or coarse-grained simulations. Nevertheless, the agreement shown here at the coarser level available to the experiments does provide validation to the simulations and provides support for our findings at the finer scales.

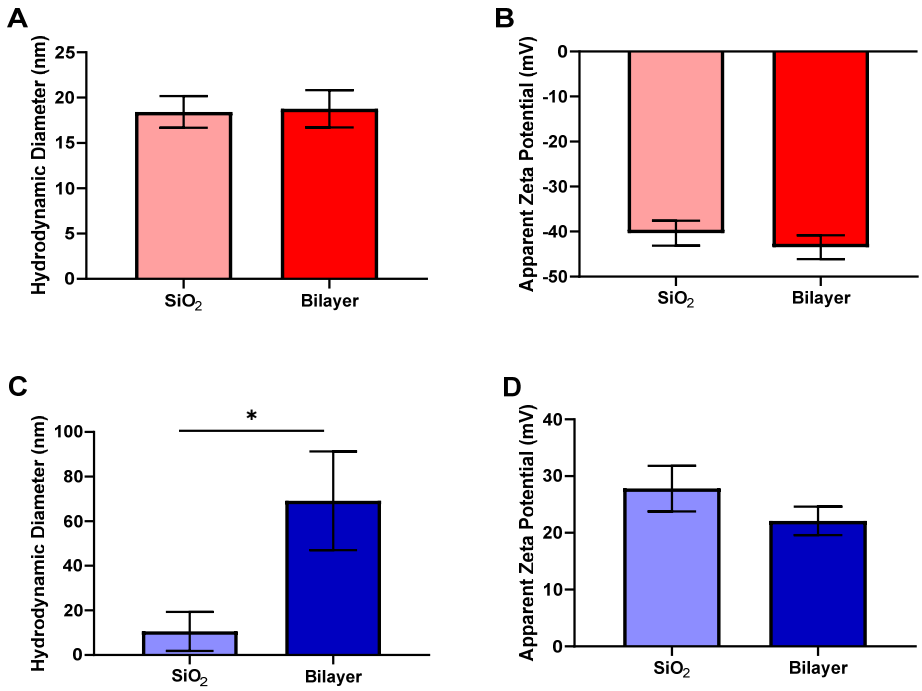

Figure 4. (A,C) Hydrodynamic diameters and (B,D) apparent zeta potentials of (A,B) MUA-AuNPs and (C,D) MUTAB-AuNPs after flowed over a bare SiO_2-coated sensor or a DOPC bilayer. Data are for triplicate experiments; error bars correspond to one standard deviation. *, $p < 0.05$.

4. Conclusion

A major finding of this work, obtained using 4-8 nm AuNPs, is the observation that self-assembled monolayers on engineered NPs can have non-uniform surface chemistry that triggers significant interactions at the nano-bio interface with biological consequences. Phospholipid extraction from zwitterionic vesicles by 14 nm MTAB-coated AuNPs has been observed earlier,[49] suggesting that even larger NPs with nearly saturated and uniformly distributed terminal headgroup ligand layers alongside smaller defects[24] strongly incorporate with lipid bilayers at long experimental time-scales. The persistence of defects in alkanethiol monolayers on NPs and planar metal films is also inevitable due to small molecule adsorbates and surface impurities, facets and unevenness of the

metal surface itself, and the assembly of ligands on such surfaces.[8,50-51] To our knowledge, reports on the influence of SAM defects on the acquisition of biomolecular coronas by NPs are limited because defect formation is inherently difficult to isolate and control through experiments. MD simulations have enabled modeling of designed defects in SAMs on planar films to show how adsorption into defects can significantly alter the native conformation of proteins.[52]

Coarse-grained DPD simulations revealed the mechanism of NP insertion, phospholipid extraction, and bilayer thinning and the structure of the corona. QCM-D experiments confirmed that long alkanethiol-coated AuNPs can attach to planar supported lipid bilayers and acquire phospholipid coronas. Hydrophobic contact between a protruding lipid tail in the bilayer and exposed hydrophobic groups on the NP surface is required to facilitate NP insertion. NP insertion into bilayers leads to bilayer curvature-dependent deformations, such as bilayer buckling and planarization for the smallest 10 nm vesicles due to their high bending resistance. No deformations in global vesicle structure are observed for larger 25 nm vesicles, suggesting a minimum vesicle size with which we can accelerate NP binding in simulations and probe local structural transformations at the NP-bilayer interface as a function of NP surface chemistry. Although the ligand charge affects the probability of NP association with bilayers—cationic NPs are more likely to insert into defect-free supported bilayers—deformations at the nano-bio interface depend on ligand structure, such as alkyl chain length. Previous coarse-grained simulations using hydrophobic bare[53] and lipid-coated[54] NPs have shown the role of hydrophobic interactions in driving NP insertion and lipid extraction from the bilayer. We have demonstrated that the presence of defects in engineered NPs can impact such transformations. The nature of defects in the SAM structure—influenced by ligand length, ligand density, NP size—together with the influence of lipid structure and the complexity of the lipid-bilayer system on lipid extraction and bilayer

thinning need to be further explored toward determining the molecular-level basis for the onset of membrane disruption and concomitant adverse biological effects.

ASSOCIATED CONTENT

Supporting Information. Simulation force-field parameters and system sizes, simulation results for all trajectories, and experimental methods and additional figures for the synthesis and characterization of nanoparticles and QCM-D. This material is available free of charge via the Internet at http://pubs.acs.org.

AUTHOR INFORMATION

Corresponding Author

*E-mail: r.hernandez@jhu.edu

ACKNOWLEDGMENTS

This work was supported by National Science Foundation under the Center for Sustainable Nanotechnology (CSN), CHE-1503408. The CSN is part of the Centers for Chemical Innovation Program. Computing resources were provided in part by the National Science Foundation through XSEDE resources under grant number CTS090079 and by the Maryland Advanced Research Computing Center.

REFERENCES

1. Aldakov, D.; Lefrancois, A.; Reiss, P. Ternary and Quaternary Metal Chalcogenide Nanocrystals: Synthesis, Properties and Applications. *J. Mater. Chem. C* **2013,** *1*, 3756-3776.
2. Smith, A. M.; Nie, S. Semiconductor Nanocrystals: Structure, Properties, and Band Gap Engineering. *Acc. Chem. Res.* **2010,** *43*, 190-200.
3. Anker, J. N.; Hall, W. P.; Lyandres, O.; Shah, N. C.; Zhao, J.; Van Duyne, R. P. Biosensing with Plasmonic Nanosensors. *Nat. Mater.* **2008,** *7*, 442-453.
4. Mayer, K. M.; Hafner, J. H. Localized Surface Plasmon Resonance Sensors. *Chem. Rev.* **2011,** *111*, 3828-3857.
5. Huang, X.; Jain, P. K.; El-Sayed, I. H.; El-Sayed, M. A. Plasmonic Photothermal Therapy (PPTT) Using Gold Nanoparticles. *Lasers Med. Sci.* **2008,** *23*, 217-228.
6. Liu, Y.; Bhattarai, P.; Dai, Z.; Chen, X. Photothermal Therapy and Photoacoustic Imaging via Nanotheranostics in Fighting Cancer. *Chem. Soc. Rev.* **2019,** *48*, 2053-2108.
7. Balazs, A. C.; Emrick, T.; Russell, T. P. Nanoparticle Polymer Composites: Where Two Small Worlds Meet. *Science* **2006,** *314*, 1107-1110.
8. Love, J. C.; Estroff, L. A.; Kriebel, J. K.; Nuzzo, R. G.; Whitesides, G. M. Self-Assembled Monolayers of Thiolates on Metals as a Form of Nanotechnology. *Chem. Rev.* **2005,** *105*, 1103-1169.
9. Dreaden, E. C.; Austin, L. A.; Mackey, M. A.; El-Sayed, M. A. Size Matters: Gold Nanoparticles in Targeted Cancer Drug Delivery. *Ther. Deliv.* **2012,** *3*, 457-478.
10. Murphy, C. J.; Vartanian, A. M.; Geiger, F. M.; Hamers, R. J.; Pedersen, J. A.; Cui, Q.; Haynes, C. L.; Carlson, E. E.; Hernandez, R.; Klaper, R. D.*, et al.* Biological Responses to Engineered Nanomaterials: Needs for the Next Decade. *ACS Cent. Sci.* **2015,** *1*, 117–123.
11. Heikkilä, E.; Martinez-Seara, H.; Gurtovenko, A. A.; Javanainen, M.; Häkkinen, H.; Vattulainen, I.; Akola, J. Cationic Au Nanoparticle Binding with Plasma Membrane-like Lipid Bilayers: Potential Mechanism for Spontaneous Permeation to Cells Revealed by Atomistic Simulations. *J. Phys. Chem. C* **2014,** *118*, 11131-11141.
12. Heikkilä, E.; Martinez-Seara, H.; Gurtovenko, A. A.; Vattulainen, I.; Akola, J. Atomistic Simulations of Anionic $Au_{144}(SR)_{60}$ Nanoparticles Interacting with Asymmetric Model Lipid Membranes. *Biochim. Biophys. Acta, Biomembr.* **2014,** *1838*, 2852-2860.
13. Goodman, C. M.; McCusker, C. D.; Yilmaz, T.; Rotello, V. M. Toxicity of Gold Nanoparticles Functionalized with Cationic and Anionic Side Chains. *Bioconjugate Chem.* **2004,** *15*, 897-900.
14. Feng, Z. V.; Gunsolus, I. L.; Qiu, T. A.; Hurley, K. R.; Nyberg, L. H.; Frew, H.; Johnson, K. P.; Vartanian, A. M.; Jacob, L. M.; Lohse, S. E.*, et al.* Impacts of Gold Nanoparticle Charge and Ligand Type on Surface Binding and Toxicity to Gram-Negative and Gram-Positive Bacteria. *Chem. Sci.* **2015,** *6*, 5186-5196.
15. Van Lehn, R. C.; Ricci, M.; Silva, P. H. J.; Andreozzi, P.; Reguera, J.; Voïtchovsky, K.; Stellacci, F.; Alexander-Katz, A. Lipid Tail Protrusions Mediate the Insertion of Nanoparticles into Model Cell Membranes. *Nat. Commun.* **2014,** *5*, 1-11.
16. Simonelli, F.; Bochicchio, D.; Ferrando, R.; Rossi, G. Monolayer-Protected Anionic Au Nanoparticles Walk into Lipid Membranes Step by Step. *J. Phys. Chem. Lett.* **2015,** *6*, 3175-3179.
17. Li, Y.; Li, X.; Li, Z.; Gao, H. Surface-Structure-Regulated Penetration of Nanoparticles across a Cell Membrane. *Nanoscale* **2012,** *4*, 3768-3775.
18. Zhang, L.; Becton, M.; Wang, X. Designing Nanoparticle Translocation through Cell Membranes by Varying Amphiphilic Polymer Coatings. *J. Phys. Chem. B* **2015,** *119*, 3786-3794.

19. Gkeka, P.; Angelikopoulos, P.; Sarkisov, L.; Cournia, Z. Membrane Partitioning of Anionic, Ligand-Coated Nanoparticles Is Accompanied by Ligand Snorkeling, Local Disordering, and Cholesterol Depletion. *PLoS Comput. Biol.* **2014,** *10*, e1004769.
20. Ghorai, P. K.; Glotzer, S. C. Atomistic Simulation Study of Striped Phase Separation in Mixed-Ligand Self-Assembled Monolayer Coated Nanoparticles. *J. Phys. Chem. C* **2010,** *114*, 19182-19187.
21. Ramalho, J. P. P.; Gkeka, P.; Sarkisov, L. Structure and Phase Transformations of DPPC Lipid Bilayers in the Presence of Nanoparticles: Insights from Coarse-Grained Molecular Dynamics Simulations. *Langmuir* **2011,** *27*, 3723-3730.
22. Chen, P.; Huang, Z.; Liang, J.; Cui, T.; Zhang, X.; Miao, B.; Yan, L.-T. Diffusion and Directionality of Charged Nanoparticles on Lipid Bilayer Membrane. *ACS Nano* **2016,** *10*, 11541-11547.
23. Lee, K.; Zhang, L.; Yi, Y.; Wang, X.; Yu, Y. Rupture of Lipid Membranes Induced by Amphiphilic Janus Nanoparticles. *ACS Nano* **2018,** *12*, 3646-3657.
24. Wu, M.; Vartanian, A. M.; Chong, G.; Pandiakumar, A. K.; Hamers, R. J.; Hernandez, R.; Murphy, C. J. Solution NMR Analysis of Ligand Environment in Quaternary Ammonium-Terminated Self-Assembled Monolayers on Gold Nanoparticles: The Effect of Surface Curvature and Ligand Structure. *J. Am. Chem. Soc.* **2019,** *141*, 4316-4327.
25. Luedtke, W. D.; Landman, U. Structure and Thermodynamics of Self-Assembled Monolayers on Gold Nanocrystallites. *J. Phys. Chem. B* **1998,** *102*, 6566-6572.
26. Ghorai, P. K.; Glotzer, S. C. Molecular Dynamics Simulation Study of Self-Assembled Monolayers of Alkanethiol Surfactants on Spherical Gold Nanoparticles. *J. Phys. Chem. C* **2007,** *111*, 15857-15862.
27. Bolintineanu, D. S.; Lane, J. M. D.; Grest, G. S. Effects of Functional Groups and Ionization on the Structure of Alkanethiol-Coated Gold Nanoparticles. *Langmuir* **2014,** *30*, 11075-11085.
28. Chew, A. K.; Van Lehn, R. C. Effect of Core Morphology on the Structural Asymmetry of Alkanethiol Monolayer-Protected Gold Nanoparticles. *J. Phys. Chem. C* **2018,** *122*, 26288-26297.
29. Frederick, M. T.; Achtyl, J. L.; Knowles, K. E.; Weiss, E. A.; Geiger, F. M. Surface-Amplified Ligand Disorder in CdSe Quantum Dots Determined by Electron and Coherent Vibrational Spectroscopies. *J. Am. Chem. Soc.* **2011,** *133*, 7476-7481.
30. Zherebetskyy, D.; Scheele, M.; Zhang, Y.; Bronstein, N.; Thompson, C.; Britt, D.; Salmeron, M.; Alivisatos, P.; Wang, L.-W. Hydroxylation of the Surface of PbS Nanocrystals Passivated with Oleic Acid. *Science* **2014,** *344*, 1380-1384.
31. Merz, S. N.; Farrell, Z. J.; Pearring, J.; Hoover, E.; Kester, M.; Egorov, S. A.; Green, D. L.; DuBay, K. H. Computational and Experimental Investigation of Janus-like Monolayers on Ultrasmall Noble Metal Nanoparticles. *ACS Nano* **2018,** *12*, 11031-11040.
32. Kranenburg, M.; Nicolas, J.-P.; Smit, B. Comparison of Mesoscopic Phospholipid-Water Models. *Phys. Chem. Chem. Phys.* **2004,** *6*, 4142-4151.
33. Gavrilov, A. A.; Chertovich, A. V.; Kramarenko, E. Y. Dissipative Particle Dynamics for Systems with High Density of Charges: Implementation of Electrostatic Interactions. *J. Chem. Phys.* **2016,** *145*, 174101.
34. Dominguez, L.; Foster, L.; Straub, J. E.; Thirumalai, D. Impact of Membrane Lipid Composition on the Structure and Stability of the Transmembrane Domain of Amyloid Precursor Protein. *Proc. Natl. Acad. Sci. U.S.A.* **2016,** *113*, E5281-E5287.

35. Li, X.; Gao, L.; Fang, W. Dissipative Particle Dynamics Simulations for Phospholipid Membranes Based on a Four-To-One Coarse-Grained Mapping Scheme. *PLoS One* **2016,** *11*, e0154568.
36. Martínez, L.; Andrade, R.; Birgin, E. G.; Martínez, J. M. Packmol: A Package for Building Initial Configurations for Molecular Dynamics Simulations. *J. Comput. Chem.* **2009,** *30*, 2157-2164.
37. Plimpton, S. Fast Parallel Algorithms for Short-Range Molecular-Dynamics. *J. Comput. Phys.* **1995,** *117*, 1-19.
38. Yan, L.-T.; Yu, X. Enhanced Permeability of Charged Dendrimers across Tense Lipid Bilayer Membranes. *ACS Nano* **2009,** *3*, 2171-2176.
39. Yang, K.; Ma, Y.-Q. Computer Simulation of the Translocation of Nanoparticles with Different Shapes across a Lipid Bilayer. *Nat. Nanotechnol.* **2010,** *5*, 579-583.
40. Cho, N.-J.; Frank, C. W.; Kasemo, B.; Höök, F. Quartz Crystal Microbalance with Dissipation Monitoring of Supported Lipid Bilayers on Various Substrates. *Nat. Protoc.* **2010,** *5*, 1096-1106.
41. Zhu, W.; von dem Bussche, A.; Yi, X.; Qiu, Y.; Wang, Z.; Weston, P.; Hurt, R. H.; Kane, A. B.; Gao, H. Nanomechanical Mechanism for Lipid Bilayer Damage Induced by Carbon Nanotubes Confined in Intracellular Vesicles. *Proc. Natl. Acad. Sci. U.S.A.* **2016,** *113*, 12374-12379.
42. Cui, Q.; Hernandez, R.; Mason, S. E.; Frauenheim, T.; Pedersen, J. A.; Geiger, F. Sustainable nanotechnology: Opportunities and challenges for theoretical/computational studies. *J. Phys. Chem. B* **2016,** *120*, 7297-7306.
43. Schmidt, C. F.; Lichtenberg, D.; Thompson, T. E. Vesicle-Vesicle Interactions in Sonicated Dispersions of Dipalmitoylphosphatidylcholine. *Biochemistry* **1981,** *20*, 4792-4797.
44. Wong, M.; Anthony, F. H.; Tillack, T. W.; Thompson, T. E. Fusion of Dipalmitoylphosphatidylcholine Vesicles at 4ºC. *Biochemistry* **1982,** *21*, 4126-4132.
45. Lin, C.-M.; Li, C.-S.; Sheng, Y.-J.; Wu, D. T.; Tsao, H.-K. Size-Dependent Properties of Small Unilamellar Vesicles Formed by Model Lipids. *Langmuir* **2011,** *28*, 689-700.
46. Huang, C.; Quinn, D.; Sadovsky, Y.; Suresh, S.; Hsia, K. J. Formation and Size Distribution of Self-Assembled Vesicles. *Proc. Natl. Acad. Sci. U.S.A.* **2017,** *114*, 2910-2915.
47. Zheng, Z.; Saar, J.; Zhi, B.; Qiu, T. A.; Gallagher, M. J.; Fairbrother, D. H.; Haynes, C. L.; Lienkamp, K.; Rosenzweig, Z. Structure-Property Relationships of Amine-Rich and Membrane-Disruptive Poly(oxonorbornene)-Coated Gold Nanoparticles. *Langmuir* **2018,** *34*, 4614-4625.
48. Wang, X.; Wang, X.; Bai, X.; Yan, L.; Liu, T.; Wang, M.; Song, Y.; Hu, G.; Gu, Z.; Miao, Q.*, et al.* Nanoparticle Ligand Exchange and Its Effects at the Nanoparticle-Cell Membrane Interface. *Nano Lett.* **2019,** *19*, 8-18.
49. Zhang, X.; Pandiakumar, A. K.; Hamers, R. J.; Murphy, C. J. Quantification of Lipid Corona Formation on Colloidal Nanoparticles from Lipid Vesicles. *Anal. Chem.* **2018,** *90*, 14387-14394.
50. Park, J.-W.; Shumaker-Parry, J. S. Strong Resistance of Citrate Anions on Metal Nanoparticles to Desorption under Thiol Functionalization. *ACS Nano* **2015,** *9*, 1665-1682.
51. Chong, G.; Laudadio, E. D.; Wu, M.; Murphy, C. J.; Hamers, R. J.; Hernandez, R. Density, Structure, and Stability of $Citrate^{3-}$ and $H_2citrate^-$ on Bare and Coated Gold Nanoparticles. *J. Phys. Chem. C* **2018,** *122*, 28393-28404.
52. Sprenger, K. G.; He, Y.; Pfaendtner, J. Probing How Defects in Self-Assembled Monolayers Affect Peptide Adsorption with Molecular Simulation. In *Foundations of Molecular*

Modeling and Simulation, Snurr, R.; Adjiman, C.; Kofke, D., Eds. Springer: Singapore, 2016; pp 21-35.
53. Li, Z.; Zhang, Y.; Ma, J.; Meng, Q.; Fan, J. Modeling Interactions between Liposomes and Hydrophobic Nanosheets. *Small* **2019**, *15*, 1804992.
54. Bai, X.; Xu, M.; Liu, S.; Hu, G. Computational Investigations of the Interaction between the Cell Membrane and Nanoparticles Coated with a Pulmonary Surfactant. *ACS Appl. Mater. Interfaces* **2018**, *10*, 20368-20376.

TOC Graphic

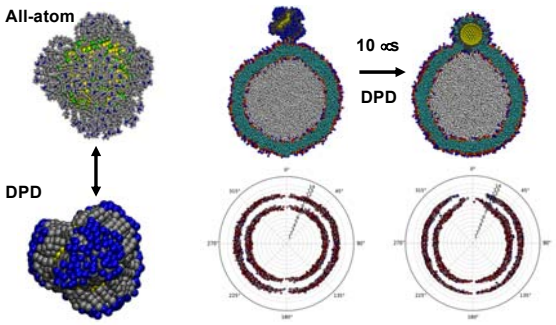

A1)

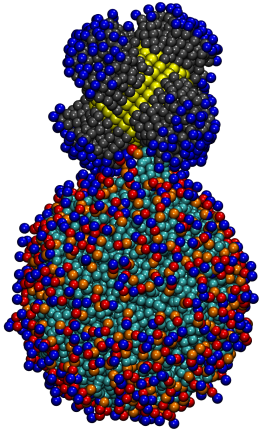

B1)

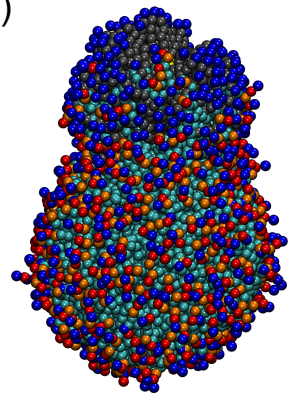

C1)

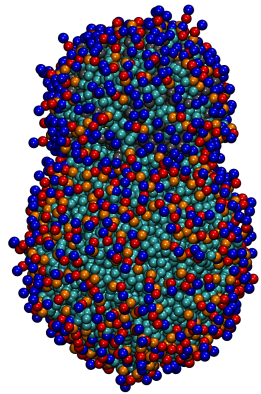

A2)

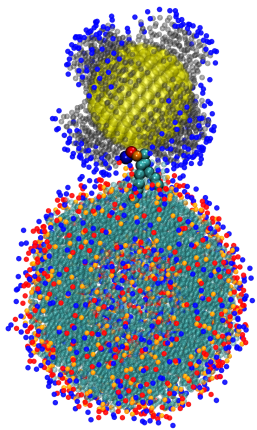

B2)

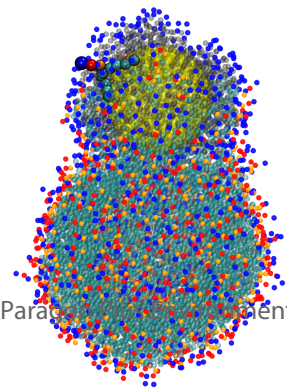

C2)

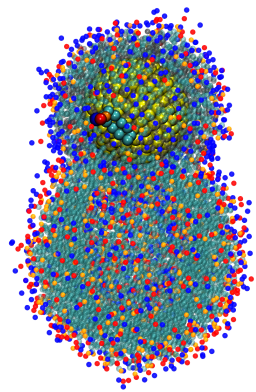

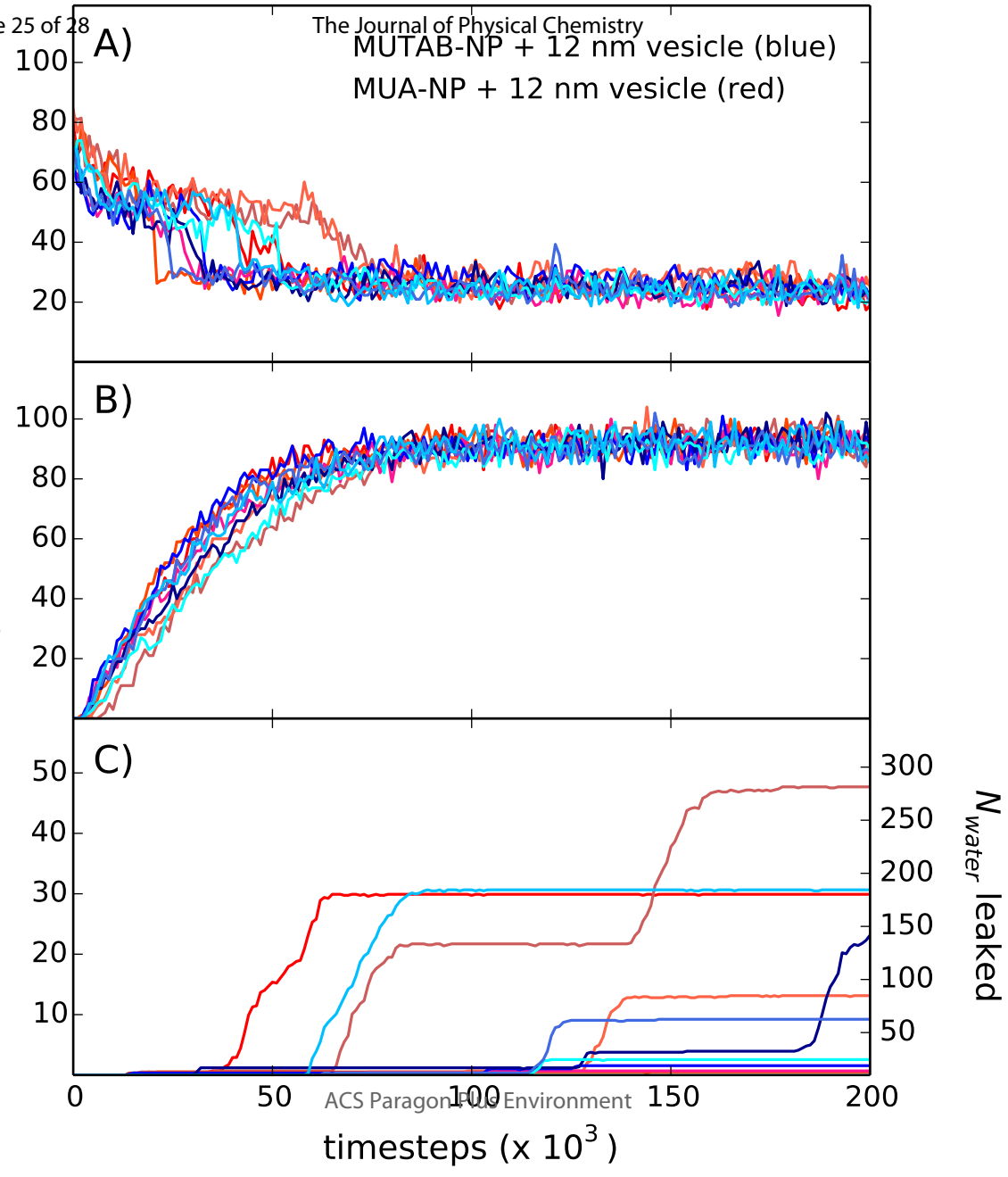
A)
MUTAB-NP + 12 nm vesicle (blue)
MUA-NP + 12 nm vesicle (red)
$d_{ligand-vesicle,COM}$ (Å)
B)
N_{lipids} extracted
C)
% N_{water} leaked
N_{water} leaked
timesteps (x 10^3)
ACS Paragon Plus Environment

A)

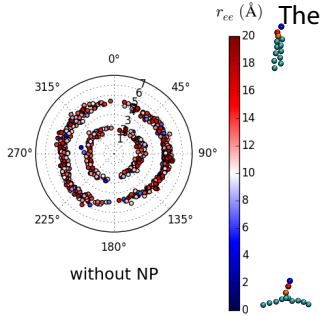

without NP

B)

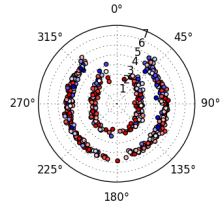

with NP

C)

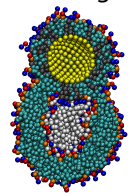

D)

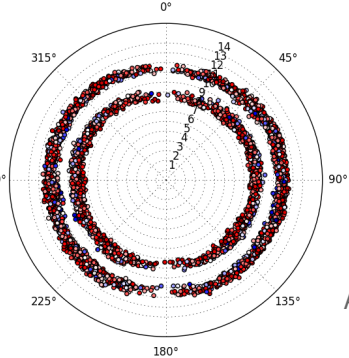

without NP

E)

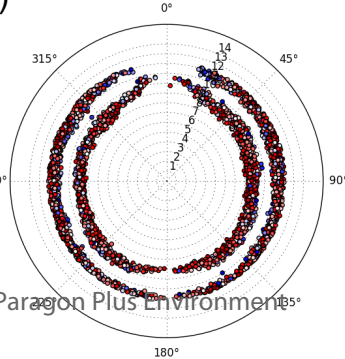

with NP

F)

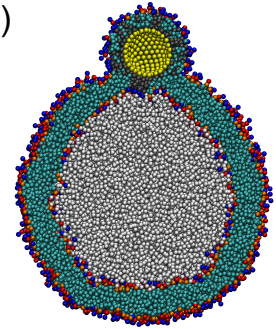

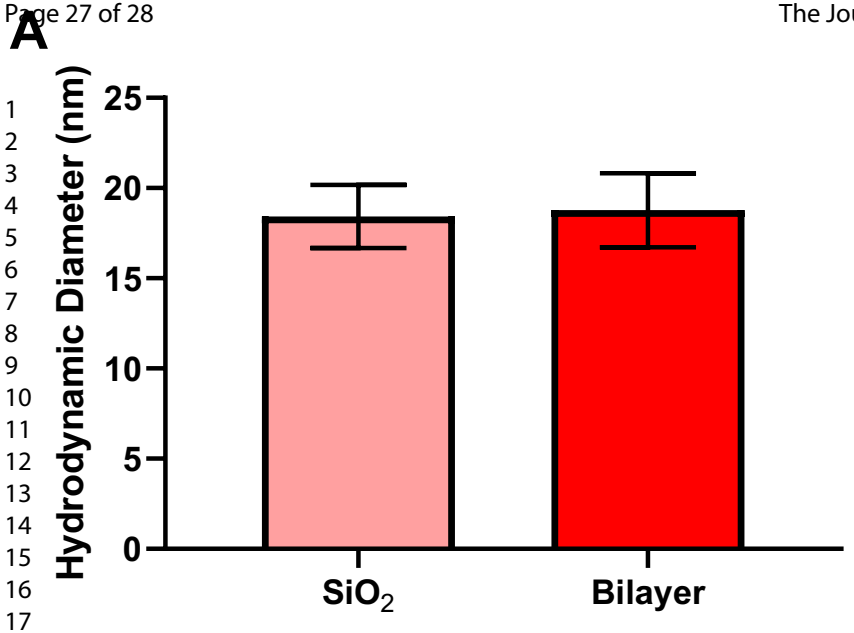
A
Hydrodynamic Diameter (nm)
25
20
15
10
5
0
SiO2
Bilayer

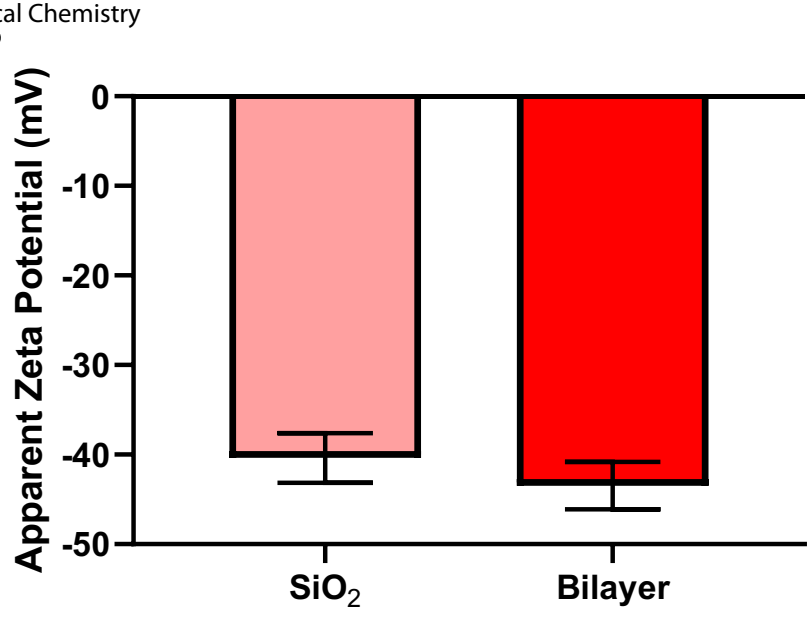
B
Apparent Zeta Potential (mV)
0
-10
-20
-30
-40
-50
SiO2
Bilayer

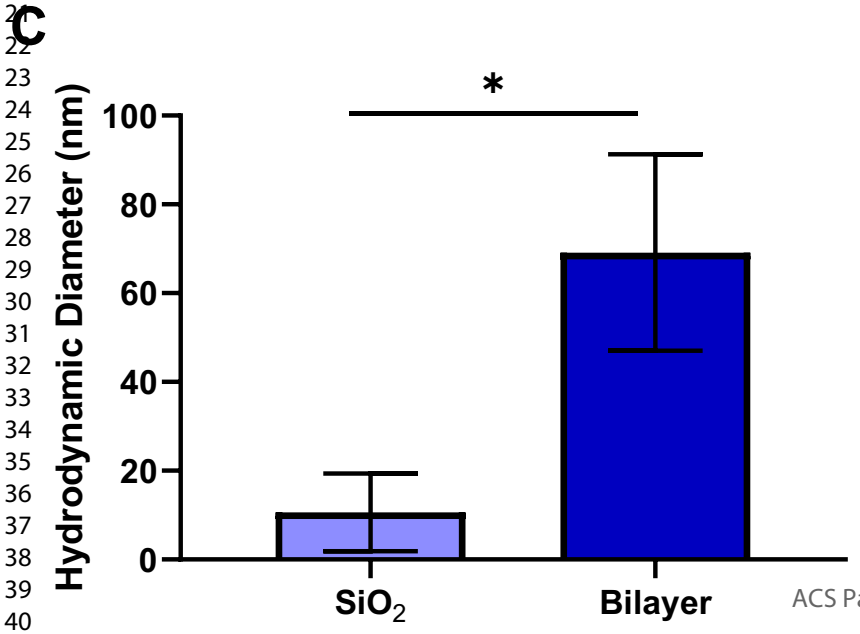
C
Hydrodynamic Diameter (nm)
*
100
80
60
40
20
0
SiO2
Bilayer

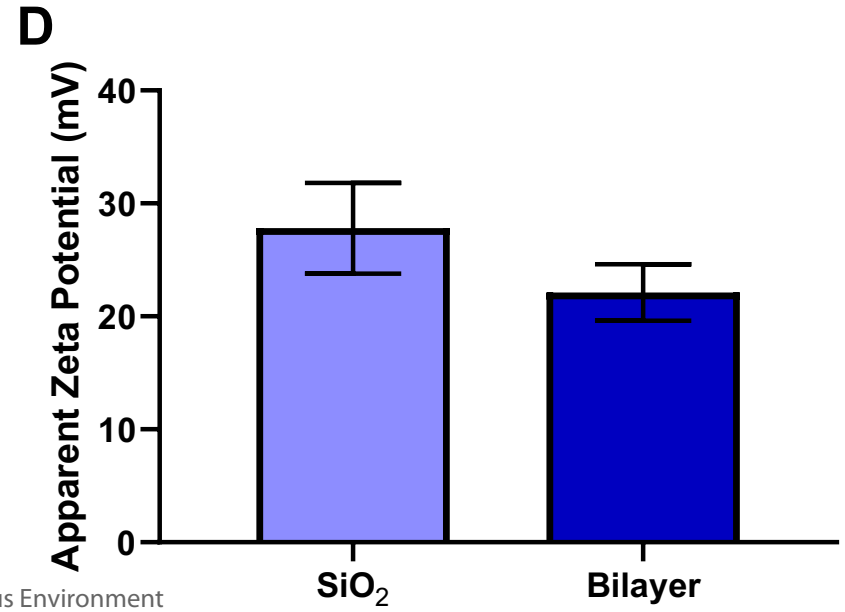
D
Apparent Zeta Potential (mV)
40
30
20
10
0
SiO2
Bilayer